PNAS

Supporting Information for

Skin-integrated systems for power efficient, programmable thermal sensations across large body areas

Minsu Park[a,1], Jae-Young Yoo[a,1], Tianyu Yang[a,b,1], Yei Hwan Jung[c,1], Abraham Vázquez-Guardado[a], Shupeng Li[d], Jae-Hwan Kim[a], Jaeho Shin[a], Woo-youl Maeng[a], Geumbee Lee[a], Seonggwang Yoo[a], Haiwen Luan[a], Jin-Tae Kim[a], Hee-Sup Shin[a], Matthew T. Flavin[a], Hong-Joon Yoon[a], Nenad Miljkovic[b], Yonggang Huang[d], William P. King[b,2], John A. Rogers[a,d,e,f,g,2]

[1]M.P., J.-Y.Y., T.Y., and Y.H.J. contributed equally to this work.

[2]Corresponding author name(s): William P. King and John A. Rogers.
Email: wpk@illinois.edu; jrogers@northwestern.edu

This PDF file includes:

Supporting texts 1 to 5
Figures S1 to S32
Tables S1 to S5
Legends for Movies S1 to S2
SI References

Other supporting materials for this manuscript include the following:

Movies S1 and S2

Supporting Information Text

Supporting Text 1. Mathematical model of the liquid pocket. The mathematical modeling of the liquid pocket is based on a previously reported pouch model (S1). *SI Appendix*, Fig. S1 shows a proposed pouch model for analysis of inflation/deflation of the bladder and numerical calculation of the volume of fluid. L is the length of the bladder when the bladder is not inflated. W is a width of the bladder. L_0 is an arc length of the cylindrical shape with radius of curvature of r and angle of 2θ when the bladder inflates. The variables P and V indicate a pressure and volume of the bladder, respectively. It is assumed that the shape of the bladder is a simple flat square when the heater is off (pocket is not inflated, $L_0 = L$) and is a pouch shape that inflates one-dimensionally (only the length changes) when the heater is on (pocket inflates, $L_0 = 2r\theta$). Hereby, the volume of the bladder can be expressed as a function of θ (degree of inflation) using known values as:

$$r \sin\theta = \frac{L}{2} \quad \text{Eq. S2}$$

$$L(\theta) = L_0 \frac{\sin\theta}{\theta} \quad \text{Eq. S3}$$

$$r = \frac{L}{2\sin\theta} = \frac{L_0}{2\theta} \quad \text{Eq. S4}$$

$$A = 2r^2\theta - Lr\cos\theta = 2\theta\left(\frac{L_0}{2\theta}\right)^2 - \left(\frac{L_0 \sin\theta}{\theta}\right)\left(\frac{L_0}{2\theta}\right)\cos\theta = \frac{{L_0}^2}{2}\left(\frac{\theta - \cos\theta\sin\theta}{\theta^2}\right) \quad \text{Eq. S5}$$

$$V(\theta) = A \times W = \frac{{L_0}^2 W}{2}\left(\frac{\theta - \cos\theta\sin\theta}{\theta^2}\right) = \frac{{L_0}^3}{2}\left(\frac{\theta - \cos\theta\sin\theta}{\theta^2}\right) \quad \text{Eq. S6}$$

With these and ideal gas equation, the liquid volume of Novec 7000 (V_l) can be calculated as (S2):

$$PV_g = n_g RT \quad \text{Eq. S7}$$

$$n_g = \frac{P}{RT} V_g \quad \text{Eq. S8}$$

$$r = \frac{L}{2\sin\theta} = \frac{L_0}{2\theta} \quad \text{Eq. S9}$$

$$m = M n_g \times 10^{-3} \quad \text{Eq. S10}$$

$$V_l = \frac{m}{\rho} = \frac{M n_g \times 10^{-3}}{\rho} = \frac{M}{\rho}\frac{P}{RT} V_g \times 10^{-3} = \frac{M}{\rho}\frac{P}{RT} \times \left\{\frac{{L_0}^3}{2}\left(\frac{\theta - \cos\theta\sin\theta}{\theta^2}\right)\right\} \times 10^{-3} \quad \text{Eq. S11}$$

with the following terms: P is a total pressure [Pa], V_g is a maximum gas volume [m^3], n_g is a mole number [mol], m is a mass [kg], M is a molar mass [g mol^{-1}], and ρ is a density [kg m^{-3}] of Novec 7000. Here, it can be assumed that the maximum inflation of the bladder occurs when the $\theta = \pi/2$, then the V_l can be calculated as:

$$V_{\mathrm{l}} = \frac{M}{\rho}\frac{P}{RT}\frac{{L_0}^3}{\pi} \times 10^{-3} \quad \text{Eq. S12}$$

$$P = P_{\mathrm{n}} + P_{\mathrm{air}} \quad \text{Eq. S13}$$

$$P_{\mathrm{n}} = exp\left[\frac{-3548.6}{T} + 22.978\right] \quad \text{Eq. S14}$$

with the following terms: P_{n} is the saturation vapor pressure of Novec 7000 (S3), and P_{air} is an atmospheric pressure (101.3 kPa). *SI Appendix*, Figs. S2*B* and *C* shows the total pressure of the bladder and the liquid volume of Novec 7000 as a function of temperature, respectively. These results suggest that 30 μL of liquid volume used to induce the maximum inflation of the bladder in the operating temperature range (300–325 K) of interest is reasonable.

Supporting Text 2. Measurement of specific cooling power of cooling gel. As described in detail in *SI Appendix*, Figs. S18 and S19, the measurements focus on the temperature of the surface of the skin phantom 20 min after application (T_{gel}), roughly 10 min after the system reaches thermal equilibrium (*SI Appendix*, Fig. S20). The change in mass of the gel divided by the measurement time ($\dot{m}$) defines the evaporation rate of the cooling gel, which is known to follow a zeroth-order kinetic model (S4). Assuming that the heat transfer only occurs along one dimension (through *z*-axis), the specific cooling power of the gel ($\dot{q}_{\mathrm{cooling}}$) can be written:

$$\dot{q}_{cooling}A = Q_{evap} + Q_{conv} \quad \text{Eq. S15}$$

where A is area of cooling gel [m^2], Q_{evap} is the heat of evaporation related to the loss of mass by evaporation [W], and Q_{conv} is heat transfer by air convection at the top surface of the gel to the ambient air [W]. The quantities Q_{evap} and Q_{conv} can be calculated as:

$$Q_{evap} = \dot{m}_{evap}\Delta H_{evap} \quad \text{Eq. S16}$$

$$Q_{conv} = h_{air}(T_{air} - T_{gel}) \quad \text{Eq. S17}$$

where ΔH_{evap} is heat of evaporation of water [J kg^{-1}] at given temperature, which can be found in online library (S5). T_{air} is the temperature of ambient air. The parameter h_{air} is the convective heat transfer coefficient [W m^2 K^{-1}), the value of which depends on the physical properties of air and the type of air convection.

A first set of experiments examines the dependence of T_{skin} on $\dot{q}_{\mathrm{cooling}}$ under free convection (v_{air} = 0 m s^{-1}) (*SI Appendix*, Fig. S21*A* and Table S2). When T_{skin} increases from 25.9 to 41.7 °C, T_{gel} increases from 22.8 to 33.7 °C. The values of $\dot{m}$ also increases from ~0.07 to ~0.15 g h^{-1}. The results for $\dot{q}_{\mathrm{cooling}}$ at each T_{skin} are 290 ± 30, 320 ± 20, 330 ± 10, 370 ± 30, 400 ± 10, and 450 ± 30 W m^{-2}, respectively. A second set of experiments defines $\dot{q}_{\mathrm{cooling}}$ for forced convection with different airflow velocities (v_{air}), at a fixed value of T_{skin}, 32 °C (*SI Appendix*, Fig. S21*B* and Table S3). When v_{air} > 0 m s^{-1}, the T_{gel} decreases rapidly from 27.6 °C to 23.7 °C but does not change significantly with further increases in v_{air}. The measured ṁ increases from ~0.01 to ~0.15 g h^{-1}, and further increase to ~0.19 g h^{-1} at v_{air}≈1.3 m s^{-1}. The resultant values of $\dot{q}_{\mathrm{cooling}}$ are 620 ± 20, 710 ± 30, 750 ± 60, and 790 ± 60 W m^{-2} for v_{air} of ~0.2, ~0.6, ~1.0, and ~1.3 m s^{-1}. A third set of experiments investigates the effect of relative humidity of ambient air (*RH*) on $\dot{q}_{\mathrm{cooling}}$ under forced convection (v_{air}≈1.3 m s^{-1}) at a fixed T_{air} of 25 °C (*SI Appendix*, Fig. S21*C* and Table S4). When

RH is 20, 40, and 60 %, T_{gel} is 21.2, 21.5, and 24.1 °C, respectively. The values of $\dot{m}$ decrease from ~0.23, ~0.18, to ~0.16 g h^{-1}. The results for $\dot{q}_{cooling}$ at each *RH* are 1100 ± 40, 880 ± 40, and 690 ± 20 W m^{-2}, respectively. A fourth set of experiments shows the dependence of T_{air} on $\dot{q}_{cooling}$ under forced convection (v_{air}≈1.3 m s^{-1}) at a fixed *RH* of 40 % (*SI Appendix*, Fig. S21*D* and Table S5). When T_{air} increases from 15 to 35 °C, T_{gel} increase from 15.7 to 28.6 °C. The values of $\dot{m}$ increases from ~0.16 to ~0.20 g h^{-1}. The resultant values of $\dot{q}_{cooling}$ are 660 ± 10, 720 ± 70, 880 ± 40, 940 ± 20, and 1100 ± 10 W m^{-2} for T_{air} of 15, 20, 25, 30, and 35 °C, respectively. The working lifetime of the cooling gel can be defined as the period until the cooling gel can no longer maintain a cooling temperature lower than the skin temperature. The result shows that the cooling power is constant for ~1.7 h, but gradually decreases, then finally becomes zero (T_{skin}≈T_{gel}) at ~5.7 h due to the depletion of water (*SI Appendix*, Fig. S21*E*). This indicates that the lifetime of the cooling gel on the skin is approximately ~5.7 h if the heater is not activated. Activating the heater will reduce this time due to accelerated evaporation of water.

Supporting Text 3. Thermal switching efficiency depending on the size of the bladder.
Using switchable thermal barrier (STB) with different dimensions can affect thermal switching performance and power efficiency. To investigate, we tested bladders with three different sizes using the measurement structure of Case I (STB_A, STB_B, and STB_C) (*SI Appendix*, Fig. S23*A* and *B*). The lateral dimensions of the heater (length & width = 17.7 mm) and the cooling gel (length & width = 12.7 mm) are fixed. The STB_A has the same dimensions as the cooling gel, smaller than the dimensions of the heater. The dimensions of STB_B are the same as those of the heater, but larger than those of the cooling gel. The dimensions of STB_C (length & width = 22.5 mm) are larger than those of the heater. The times and energies for inducing a similar change in T_{skin} (ΔT≈13 °C, from 27 °C to 40 °C) upon the application of a fixed power (≈0.8 W) are ~20 s (~16 J), ~13 s (8.9 J), and ~22 s (~17 J) for STB_A, STB_B, and STB_C, respectively (*SI Appendix*, Fig. S23*C*–*E*). Current and electrical power profiles over time for each STB appear in *SI Appendix*, Fig. S23*F*. For the STB_A compared to the STB_B, the area of the bladder that contacts the cooling gel is increased and the area of the bladder that contacts the heater is decreased due to the reduced size of the bladder. In the case of STB_C, uniform heating or expansion of the bladder becomes less efficient if the size of the bladder is larger than that of the heater.
Similar to the experiments in Fig. 2*B*–*D*, the power required to reach a defined T_{skin} in a fixed period of time are measured for the three different sized bladders (*SI Appendix*, Fig. S24). Since the expansion behavior of the bladder is different for each case, a similar temperature rise in T_{skin} can be obtained by applying different applied voltages (*SI Appendix*, Fig. S24*A*). Cooling curves that rely on passive cooling showed slight differences, but all three cases showed similar trends (*SI Appendix*, Fig. S24*B*). The power and energy are calculated as ~1.5 W (~10 J), ~1.2 W (~8.4 J), and ~1.3 W (~8.8 J) for STB_A, STB_B, and STB_C, respectively (*SI Appendix*, Fig. S24*C* and *D*). These results indicate that careful dimensional design is needed in the structure of a thermal module, as the efficiency of inflation/deflation of bladder depends on the size of the bladder in addition to the passive cooling power of the cooling gel.

Supporting Text 4. Evaluation of thermoregulating performance in environmental chamber.
Additional testing in an environmental chamber reveals the thermoregulating performance of the system at very low or very high air temperatures. In the chamber, the skin phantom represents skin at a temperature of ≈32 °C using a benchtop setup (*SI Appendix*, Fig. S28*A*) illustrated in *SI Appendix*, Fig. S18 and S19. The device was attached to the phantom, and the temperatures of the thermoregulation-activated thermal module (T_{skin}, active) and the thermoregulation-inactivated thermal module (T_{skin}, inactive) were simultaneously monitored. The temperature of the active device was set to ≈32 °C for thermoregulation. The initial temperature of ambient air (T_{air}) is set to 27 °C, and it gradually decreases or increases when the temperature is set to 1.5 °C or 45 °C by PID controller installed in the chamber. Results show that the T_{skin} remains at a constant value (≈32 °C) with an active device even at T_{air}≈1.5 °C, but significantly decreases to ≈15 °C with an inactive device (*SI Appendix*, Fig. S28*B*). In the case of T_{air}≈45 °C, the T_{skin} remains at the set point (≈32 °C) with an active device as T_{air} increases from 27 °C to ≈43 °C during the initial 30 min. The temperature then slightly increases (≈33 °C) after an additional 10 min, due to the

reduced cooling power of the passive cooling gel. By contrast, the T_{skin} increases to ≈41 °C on the inactive device as the T_{air} increases (*SI Appendix*, Fig. S28*C*).

Supporting Text 5. Sensory expansion for thermal recognition of remote objects. This mode of operation allows a user to thermally sense remote objects, without touch (Fig. 6*C*–*N*). Overheating of a laptop can be evaluated through visual information in a thermal image (Figs. 6*C* and *D*). Pixelization of the image yields information to reconstruct a similar pattern of heating in a device mounted on the lower arm. In this process, the maximum temperature of 34.4 °C and the thermal distribution (Fig. 6*E* and *F*) corresponded to average values in the IR image in Fig. 6*D*. Other examples include sensing of a soldering heat gun and a chemically reactive liquid in various environments as shown in Fig. 6*G*–*N*. A confusion matrix shows that users can distinguish different intensities of heating stimulation at a fixed area (8.33 cm^2), with average perception accuracies for temperatures 30, 35, and 44 °C were 97.5, 81.5 %, and 92.9 %, respectively (*SI Appendix*, Fig. S29). Based on the literature information on temperature sensitivity mapping (S6), and on the distribution of thermoreceptors (S7), desirable locations for attaching our t-eVR device are the upper body, rather than the lower body, especially the chest, back, and abdomen.

a

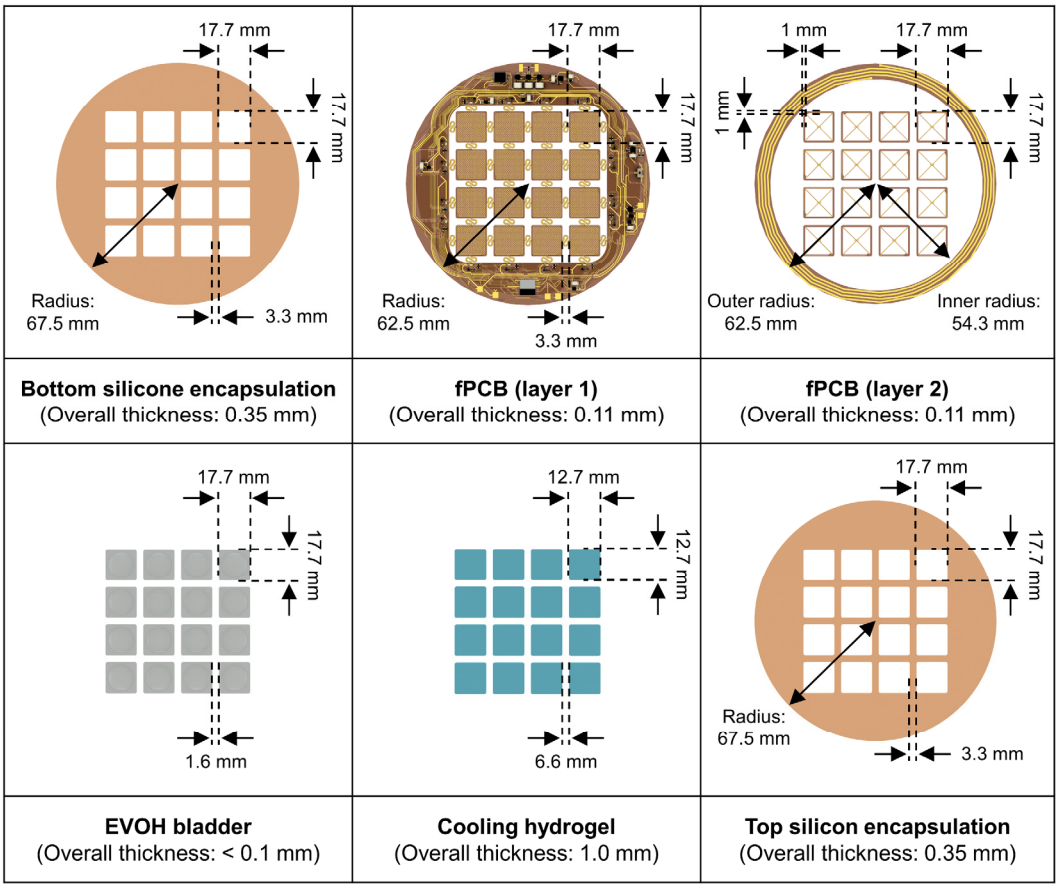

b

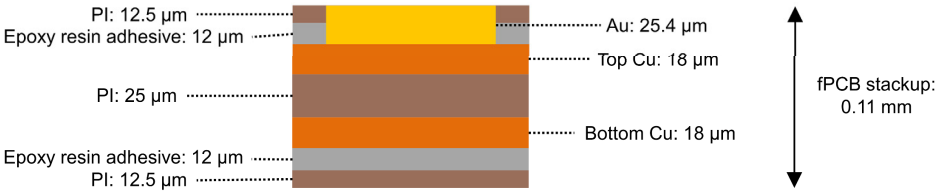

Fig. S1. (a) Design and dimensions of each layer in t-eVR system. (b) Structure of fPCB stackup.

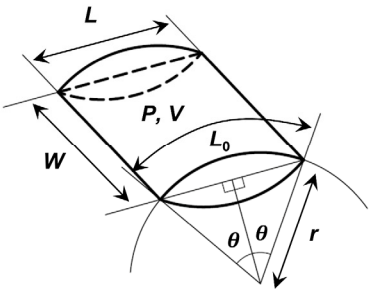

Fig. S2. Model of the switchable thermal barrier (STB).

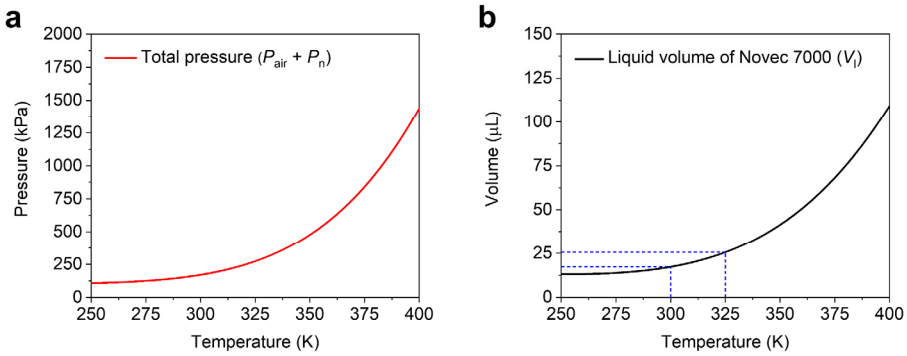

Fig. S3. (a) Pressure generated in the switchable thermal barrier (STB) as a function of temperature. (b) Liquid volume of Novec 7000 as a function of temperature.

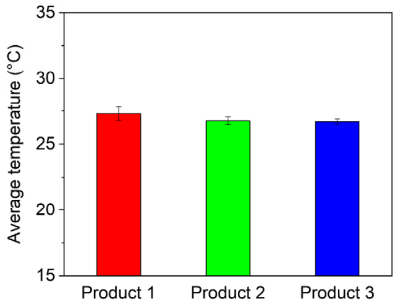

Fig. S4. Average temperature of a super-absorbent polyacrylate-based cooling gel on a skin phantom for 3 h. The temperatures of the ambient air and the skin phantom are 22 °C and 32 °C, respectively. Relative humidity of the ambient air is ~45 %. Measurements of temperature were performed under the natural convection condition. Product 1–3 are commercially available cooling gel sheets manufactured by Kobayashi Pharmaceutical Co Ltd.

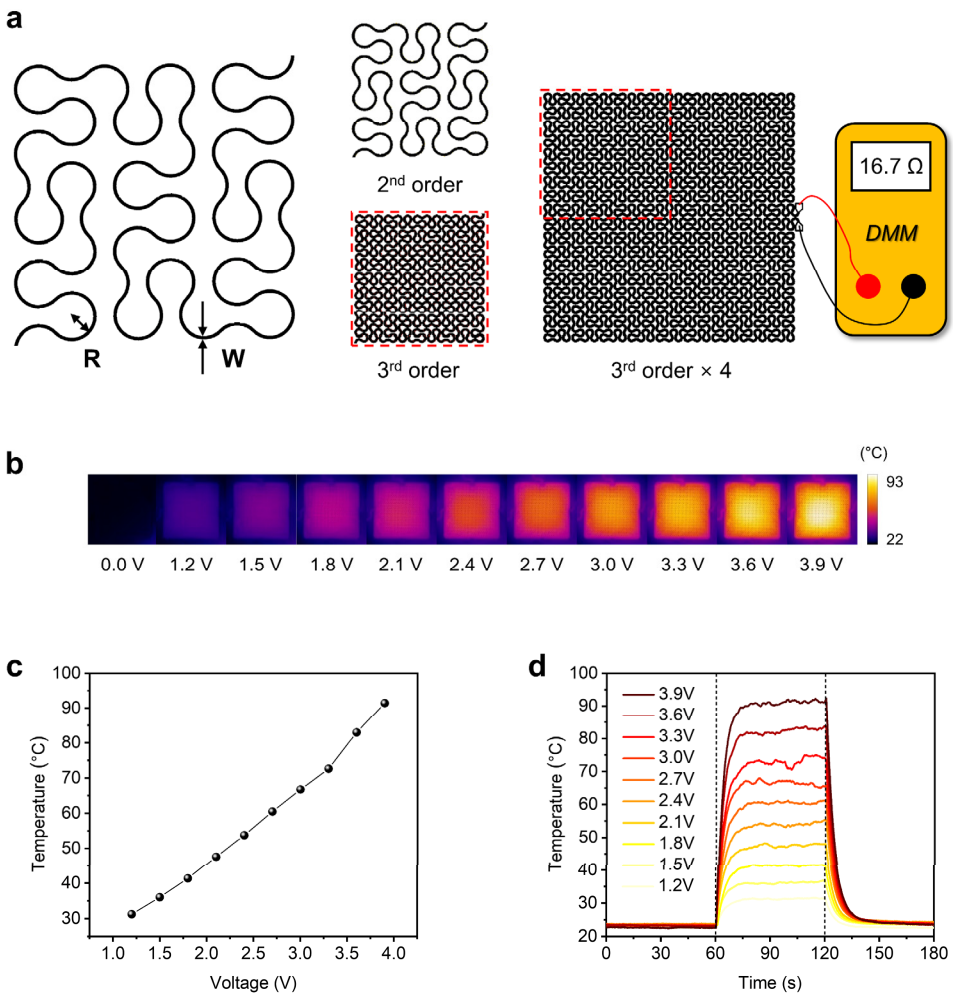

Fig. S5. (a) Geometries and dimensions of Peano fractal-shaped Cu traces. The *R* and *W* for the 2nd order Peano curve are 0.62 and 0.06 mm, respectively. The *R* and *W* for 3rd order Peano curve are 0.19 and 0.06 mm, respectively. The geometry of a single heater in the final system consists of a connection of 4×3rd order Peano curves, and the resistance value measured with a digital multimeter (DMM) is 16.7 Ω. (b–d) Series of IR images (b), maximum temperature values (c), and temperature values as a function of time (d) for a single heater with increasing applied voltage.

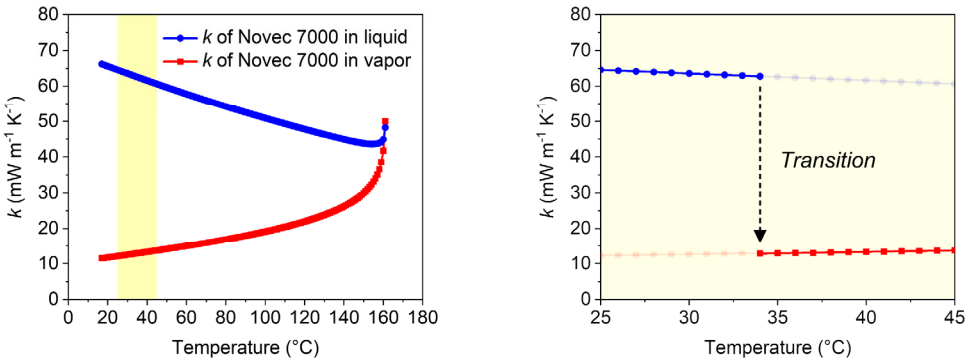

Fig. S6. Thermal conductivity (k) of Novec 7000 in the liquid and vapor phase in saturation state as a function of temperature.

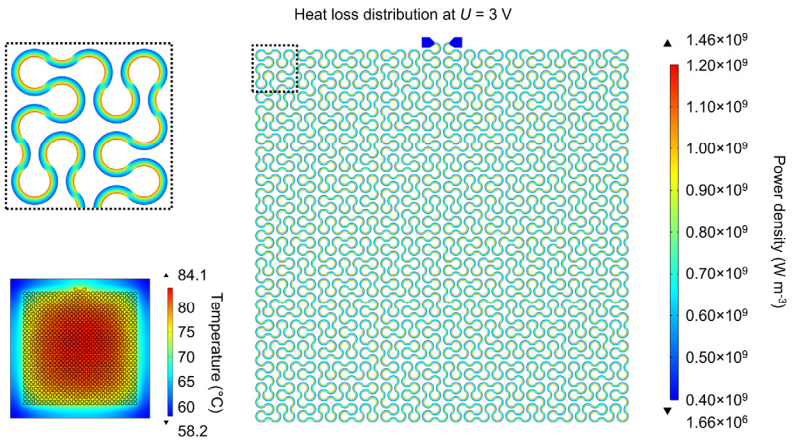

Fig. S7. Finite element analysis (FEA) results for Joule heating in a Peano fractal-shaped copper trace.

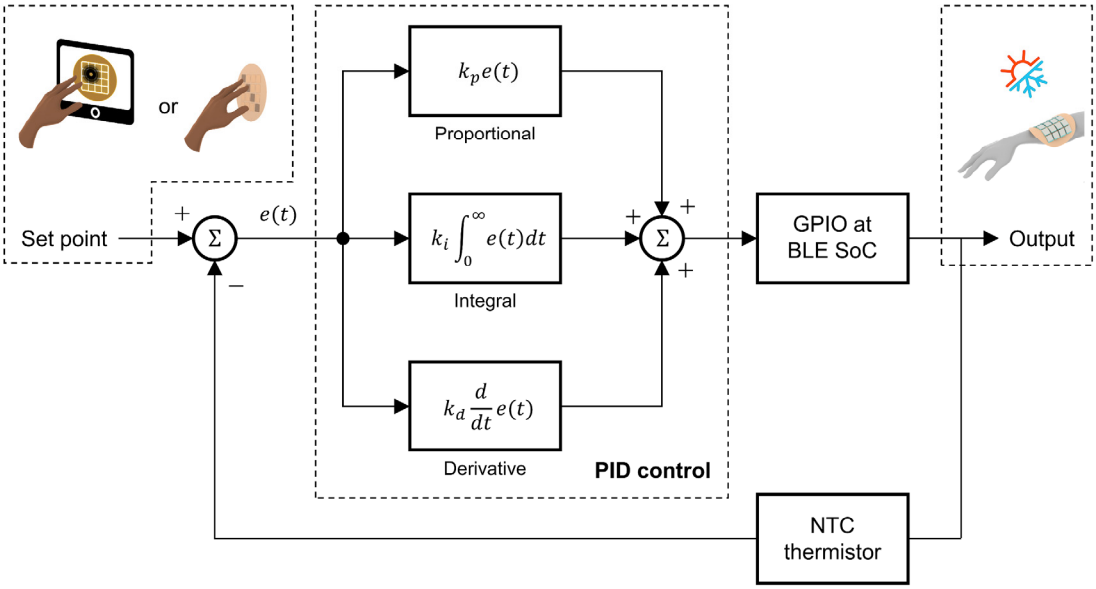

Fig. S8. Block diagram of proportional-integral-derivative (PID) temperature control. The set point indicates a target value of temperature directly entered by touching the screen of a mobile device (e.g., smartphone), or of a device. The quantity *e*(*t*) corresponds to the temperature difference between the set point and the output.

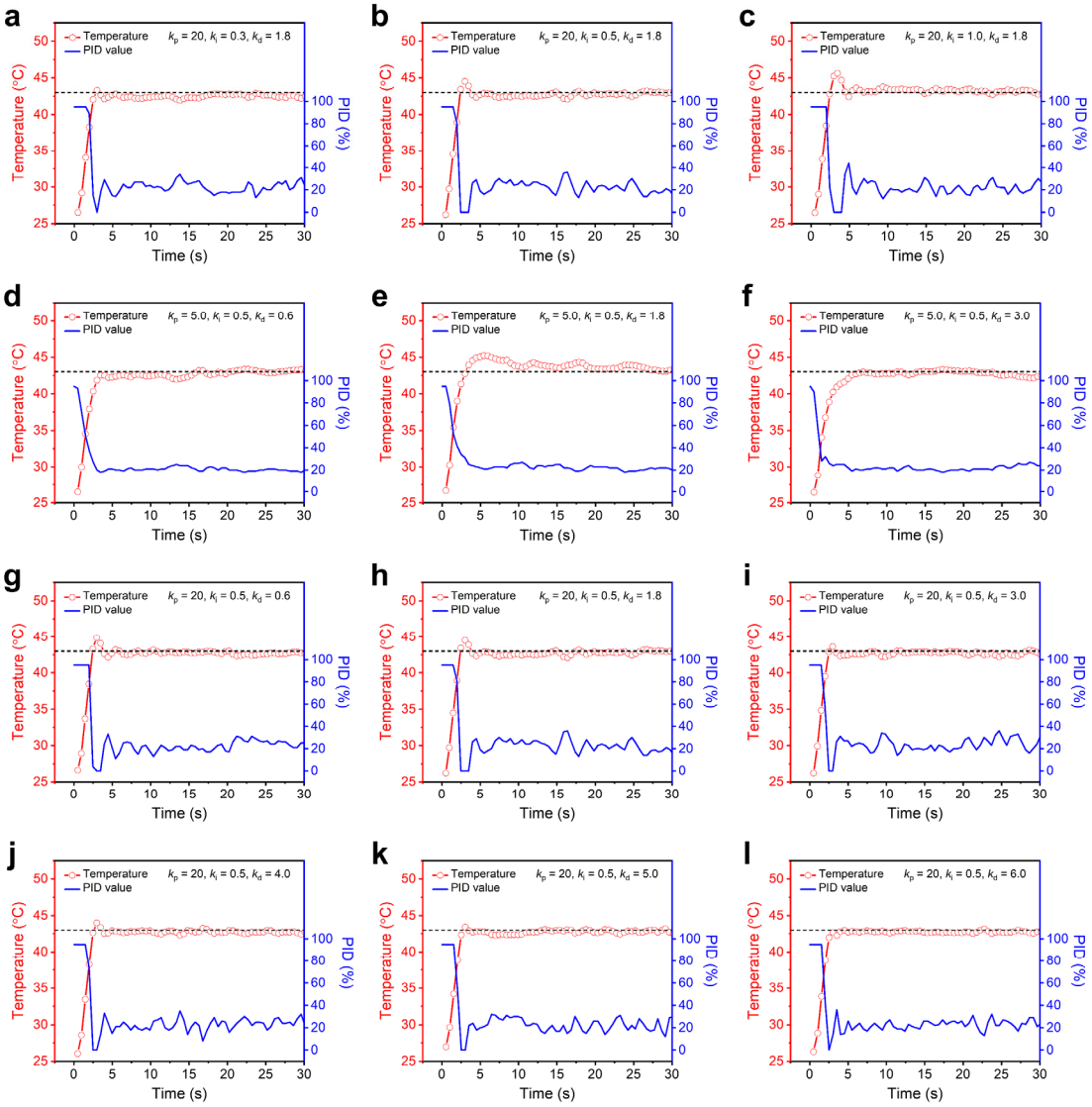

Fig. S9. (a–l) Temperature profile and PID value of the heater for different gain values for proportional (k_p), integral (k_i), and derivative (k_d).

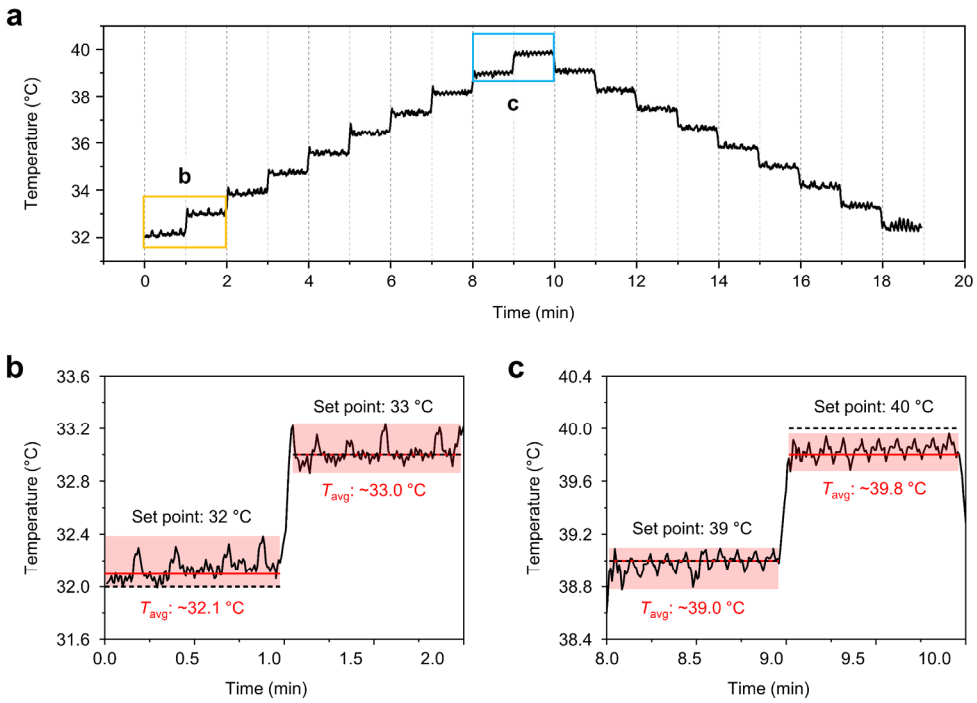

Fig. S10. (a) Time-dependent temperature profile of a thermal module programmed to modulate the temperature in a stepwise fashion. (b and c) Temperature profile of a thermal module when the set point changes from (b) 32 °C to 33 °C, and (c) 39 °C to 40 °C. The gain values for proportional (k_p), integral (k_i), and derivative (k_d) are 20, 0.5, and 6.0, respectively.

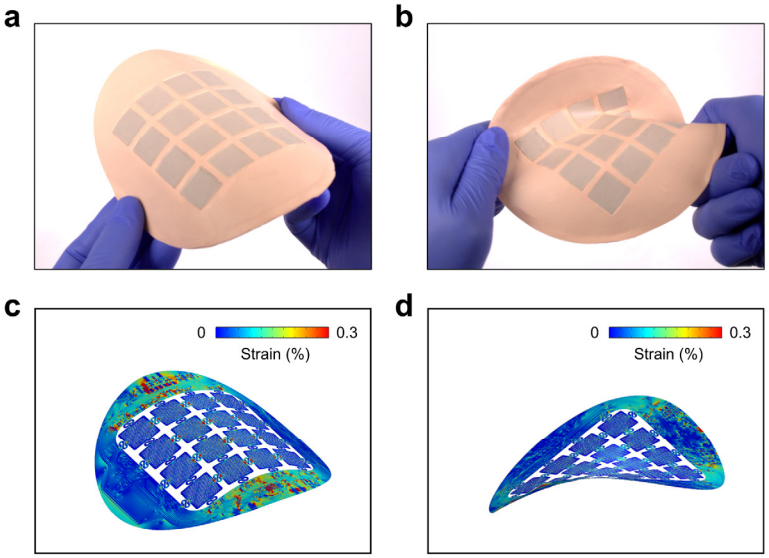

Fig. S11. (a and b) Photographs of the thermally controlled epidermal VR (t-eVR) system in various states of mechanical deformation such as bending and twisting. (c and d) Finite element analysis of the mechanics for these cases.

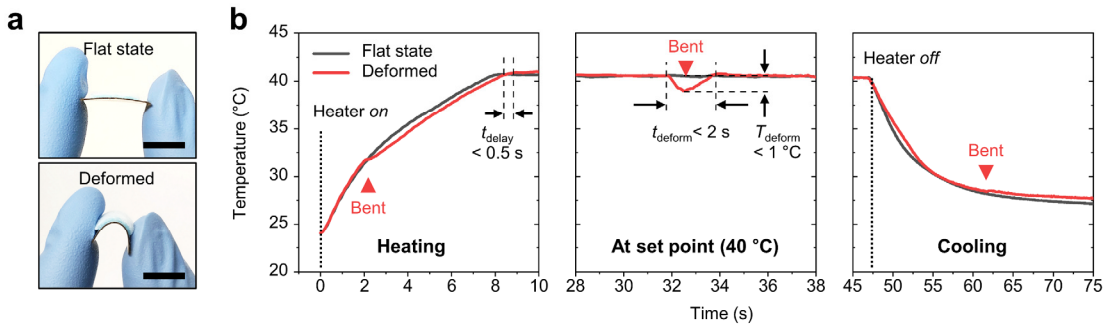

Fig. S12. (a) Photograph of a thermal module bent between the fingertips. Scale bar is 10 mm. (b) Temperature of the thermal module as a function of time when the device is bent during heating (left), maintaining at the set point (center), and cooling (right).

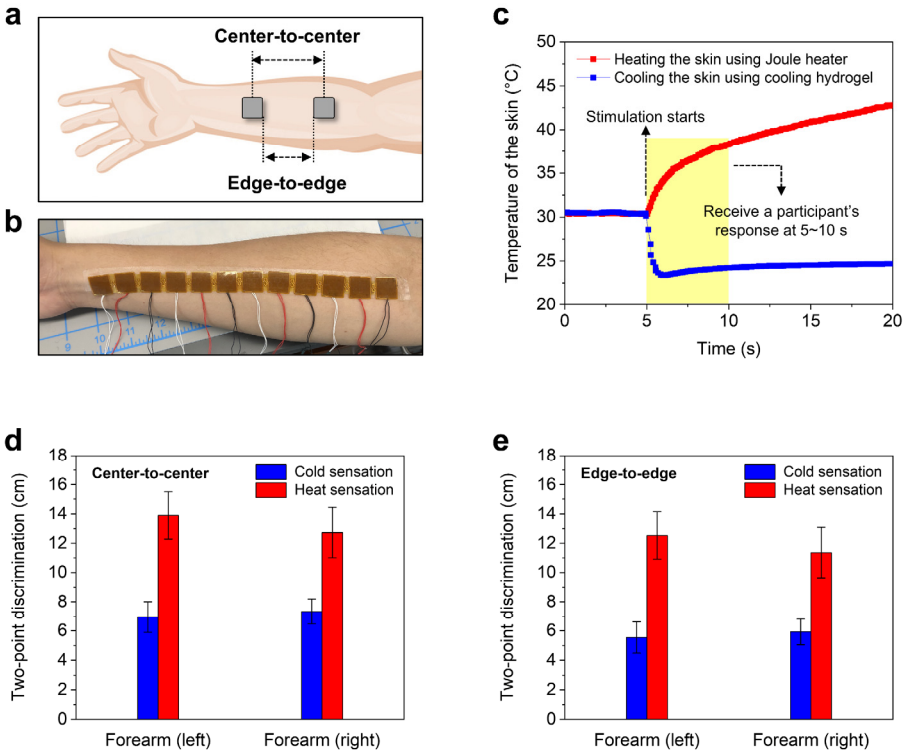

Fig. S13. (a) Schematic illustration of two-point discrimination (2PD) tests performed on the forearm for thermal stimulation using a heater of polyimide/copper/polyimide and a cooling hydrogel. (b) Photograph of a device with 12 heaters connected in series mounted on the forearm. The stimulation area of a single heater is (14.4×14.4 mm^2). The center-to-center distance between each heater is 19.3 mm, and the edge-to-edge distance between adjacent heaters is 5.0 mm. (c) Temperature of the skin as a function of time after initiation of thermal stimulation defined by operation of the Joule heater with a power of 0.67 W. This operation causes the temperature of the skin to reach ~38.3 °C from 30.4 °C within 5 s with an average rate of temperature change of 1.6 °C s^{-1}. The cold stimulation follows from evaporative cooling of the hydrogel, to decrease the temperature of the skin to ~23.4 °C from 30.4 °C within 1 s with an average rate of temperature change of 6.9 °C s^{-1}. The temperature then remains a ~24.0 °C during evaluation of the participant's response. (d and e) The 2PD results for the distance between the centers of each stimulation site (d), and the distance between the edges of each site (e). Tests were performed with five healthy adult participants (age, 30~36 years; four males and one female). The ambient air temperature and relative humidity were 22 °C, and 45 %, respectively.

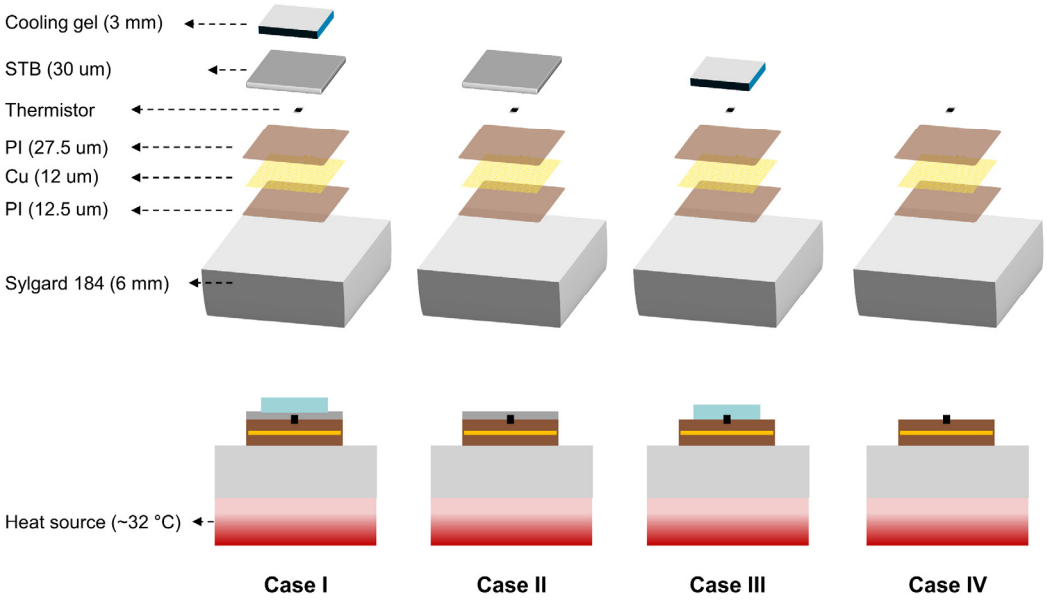

Fig. S14. Exploded view schematic illustration and measurement conditions for each case. The switchable thermal barrier (STB) consists of a fluid filled bladder formed from two aluminized ethylene vinyl alcohol (EVOH)-based films heat sealed around their edges. A surface-mounted device (SMD) type thermistor chip was used for temperature sensing (length: 1.0 ± 0.1 mm, width: 0.50 ± 0.05 mm, thickness: 0.50 ± 0.05 mm). PI: polyimide, Cu: copper.

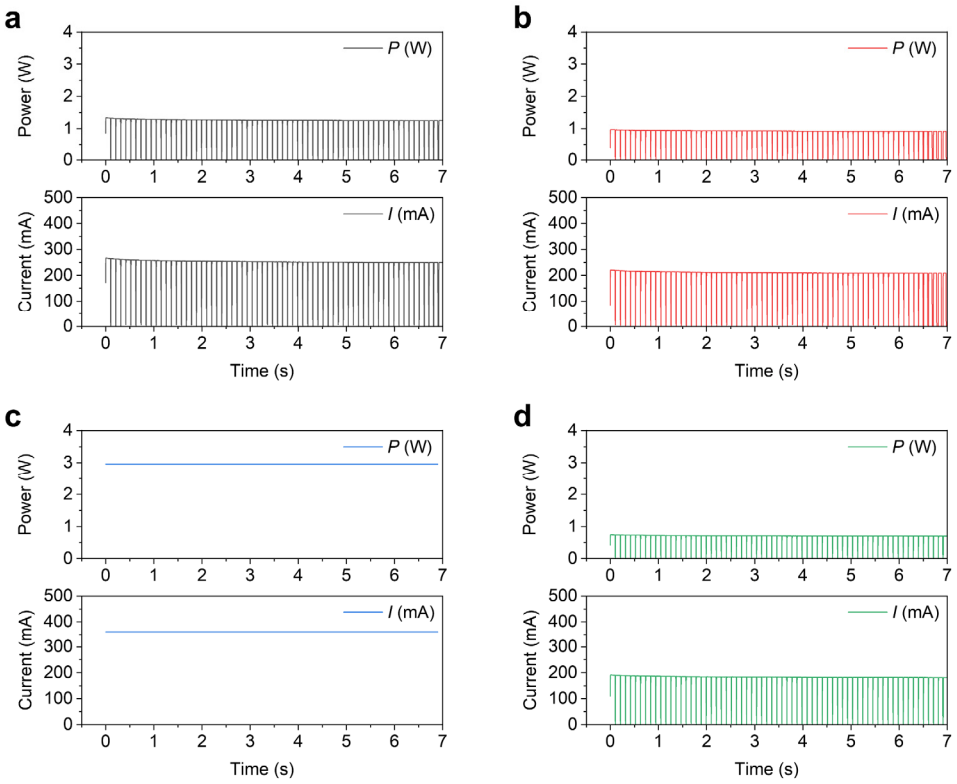

Fig. S15. (a–d) Current and power consumption ($0 \leq t \leq 7$ s) needed to induce $\Delta T \approx 13$ °C for Case I (a), Case II (b), Case III (c), and Case IV (d), respectively. The current consumption was measured using a Power Profiler Kit II (PPK2) board by connecting the device for each case, and the power consumption was calculated as: $P = IV$. The applied voltage was 5.0, 4.4, 8.2, and 3.9 V for Case I, II, III, and IV, respectively. Note that a DC voltage was applied to the structure in Case IV without pulse-width modulation (PWM) to achieve the same level of heating power as with other structures.

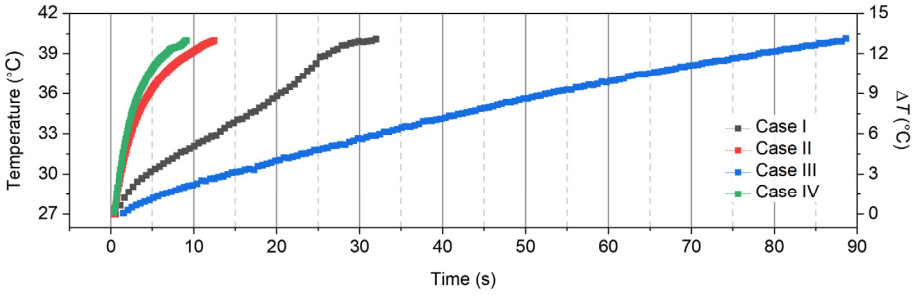

Fig. S16. Temperature as a function of time for Cases I–IV.

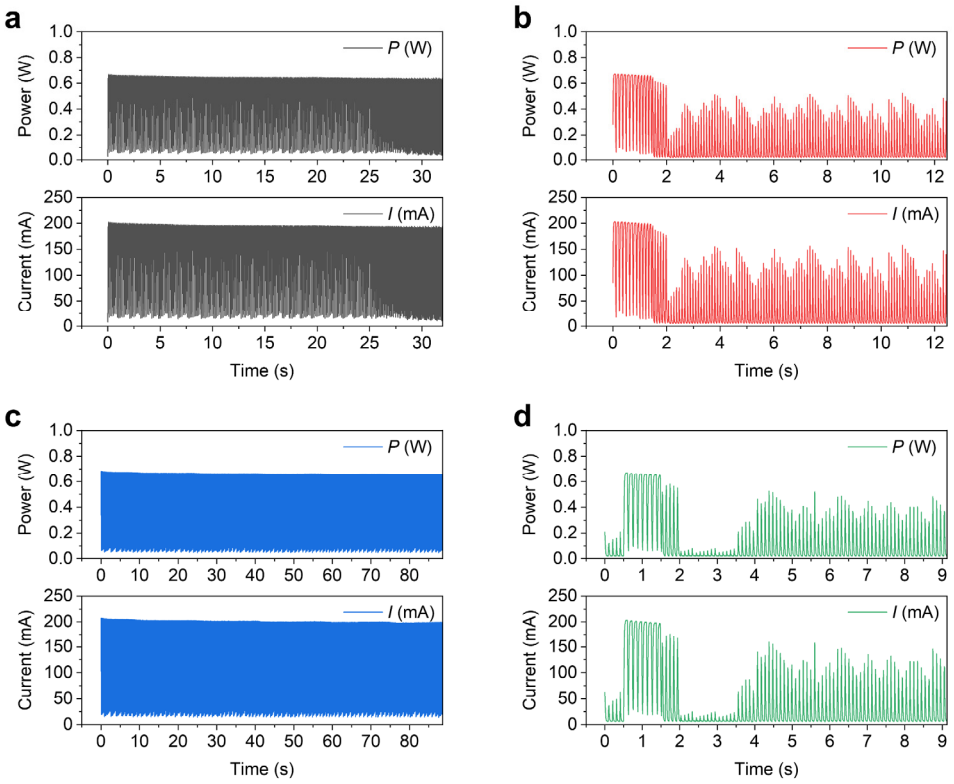

Fig. S17. (a–d) Current and power consumption (0≤ *t* ≤90 s) for Case I (a), Case II (b), Case III (c), and Case IV (d), respectively. The current consumption was measured using a Power Profiler Kit II (PPK2) board by connecting the device for each case, and the power consumption was calculated as: $P = IV$. The applied voltage was 3.3 V. The initial and final (set point) temperature in each structure was 27 °C and 40 °C, respectively. The time required to reach the set point from the initial temperature was ~32 s, ~13 s, ~89 s, and ~9 s, for Case I, II, III, and IV, respectively.

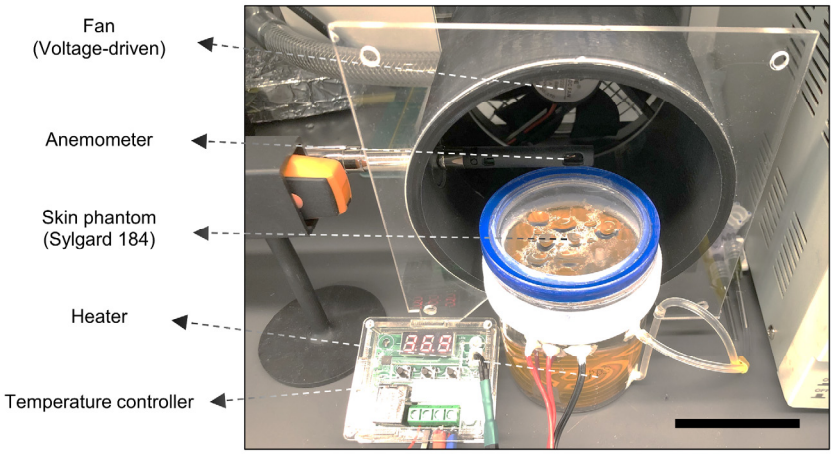

Fig. S18. Photograph of benchtop setup for measuring heating/cooling performance of the thermal module and specific cooling power of the cooling gel.

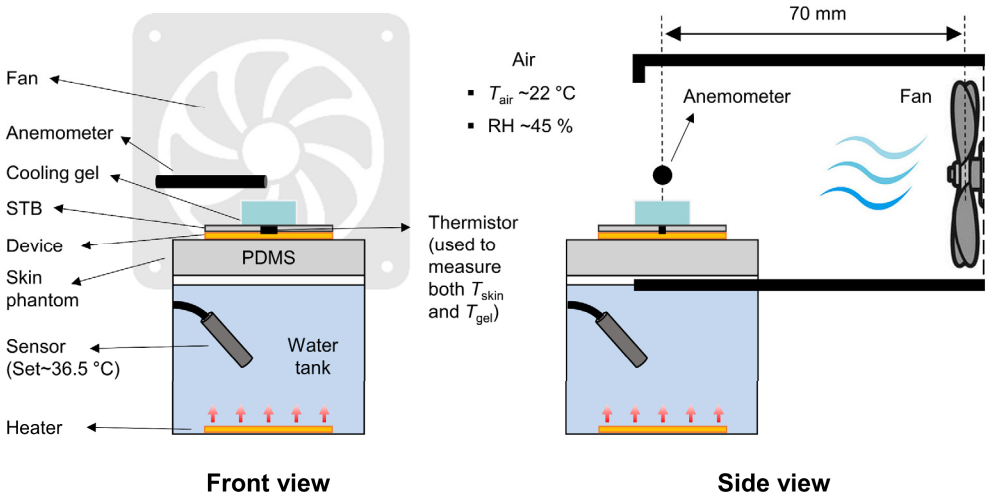

Fig. S19. Schematic illustration of the benchtop setup from front (left) and side (right) views.

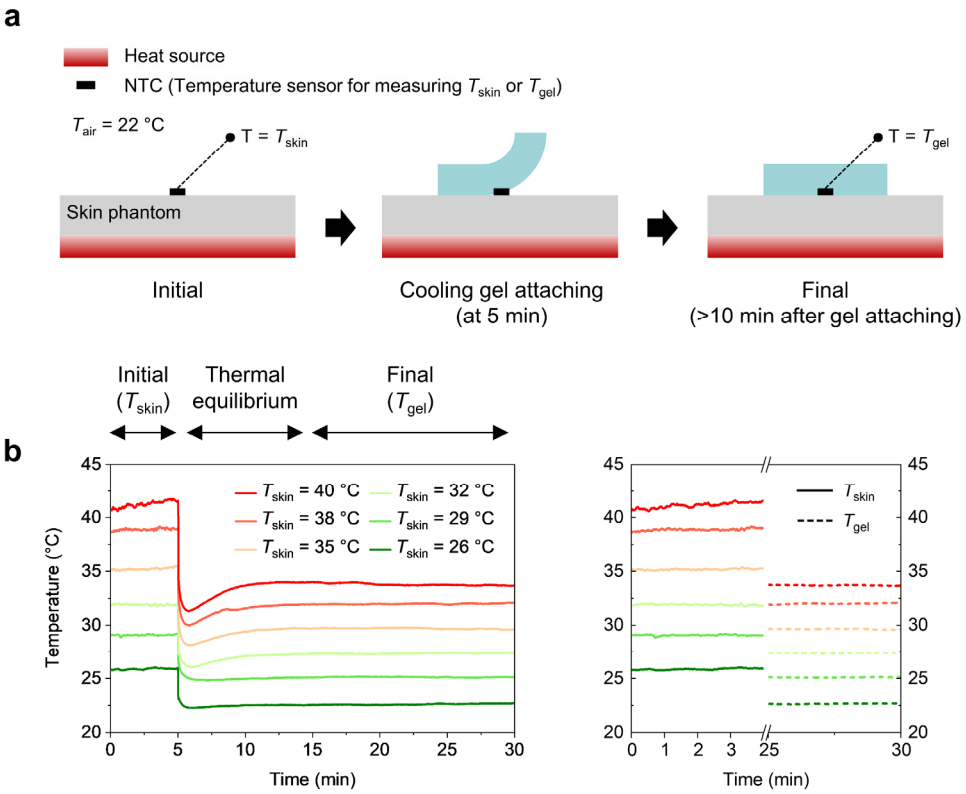

Fig. S20. (a) Method of monitoring the temperature using a benchtop setup. The initial measured temperature defines the skin temperature (T_{skin}). ~10 min after attaching a cooling gel, the final measured temperature defines the cooling gel temperature (T_{gel}). (b) Variation of temperature with time (left). The temperatures measured for the first 5 min represent 6 different T_{skin} (solid lines) that are set by controlling the heat source, and those for the last 5 min represent the resultant T_{gel} (dashed lines) (right).

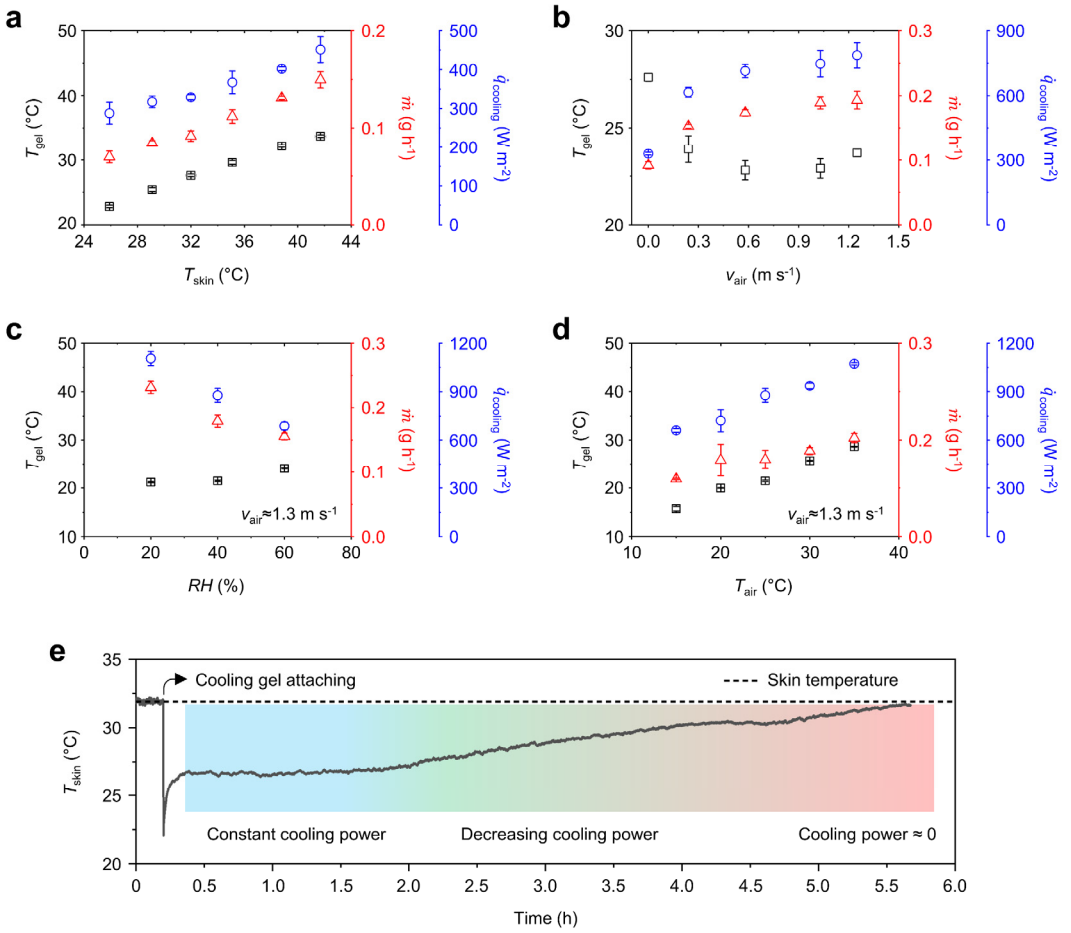

Fig. S21. (a–d) Temperature of the cooling gel (T_{gel} in °C), evaporation rate of the cooling gel ($\dot{m}$ in g h^{-1}), and specific cooling power ($\dot{q}$ in W m^{-2}) of the system in Case I at different skin temperatures (T_{skin}) (a), velocities (v_{air}) (b), relative humidity (RH in %) (c), and temperatures (T_{air} in °C) (d) of ambient air. Calculations of $\dot{q}$ in (d and e) are based on the forced convection condition as the environmental chamber controls the temperature and relative humidity with a constant airflow (v_{air}≈1.3 m s^{-1}). (e) Temperature of skin (T_{skin} in °C) over time before (0–0.2 h) and after (0.2–5.7 h) attaching the cooling gel. The temperature and relative humidity of the ambient air distant from the cooling gel are 22 °C and 45 %, respectively.

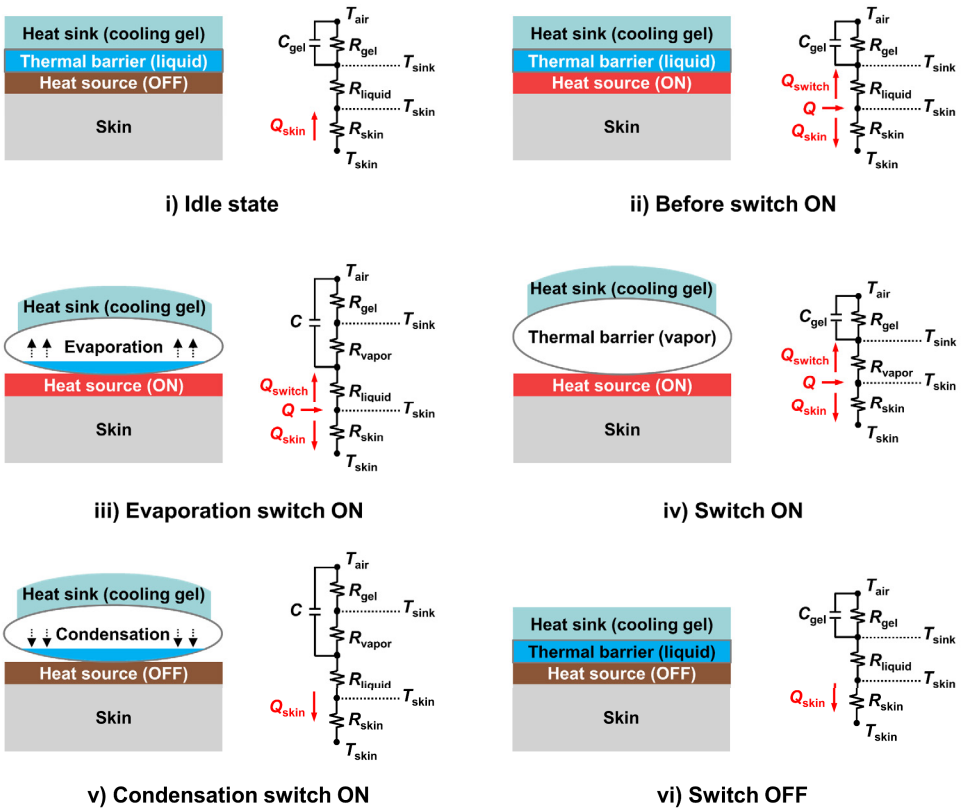

Fig. S22. Thermal resistance model that captures the mechanisms of the thermal switching system.

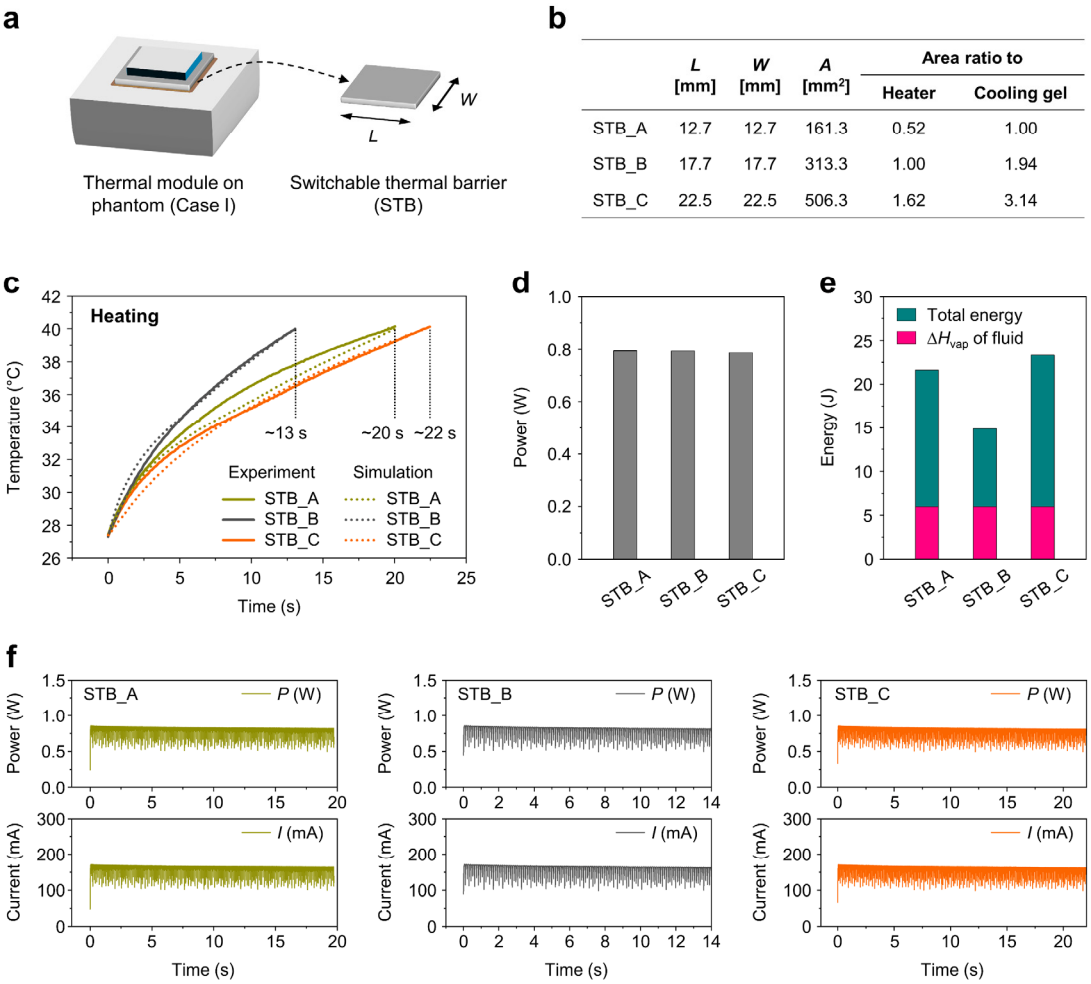

	L [mm]	W [mm]	A [mm²]	Area ratio to Heater	Area ratio to Cooling gel
STB_A	12.7	12.7	161.3	0.52	1.00
STB_B	17.7	17.7	313.3	1.00	1.94
STB_C	22.5	22.5	506.3	1.62	3.14

Fig. S23. (a) Schematic illustration of the benchtop temperature measurement setup using different lateral sizes of switchable thermal barrier (STB). (b) Dimensions of each STB. (c–f) Temperature as a function of time (c), average power for inducing $\Delta T \approx 13$ °C (d), total energy consumption (e), and current and power consumption (f) for Case I using STB_A, STB_B, and STB_C, respectively. The applied voltage was 5.0 V. The initial and final (set point) temperature in each structure was 27 °C and 40 °C, respectively. The time required to reach the set point from the initial temperature was ~20 s, ~13 s, and ~22 s, for STB_A, STB_B, and STB_C, respectively.

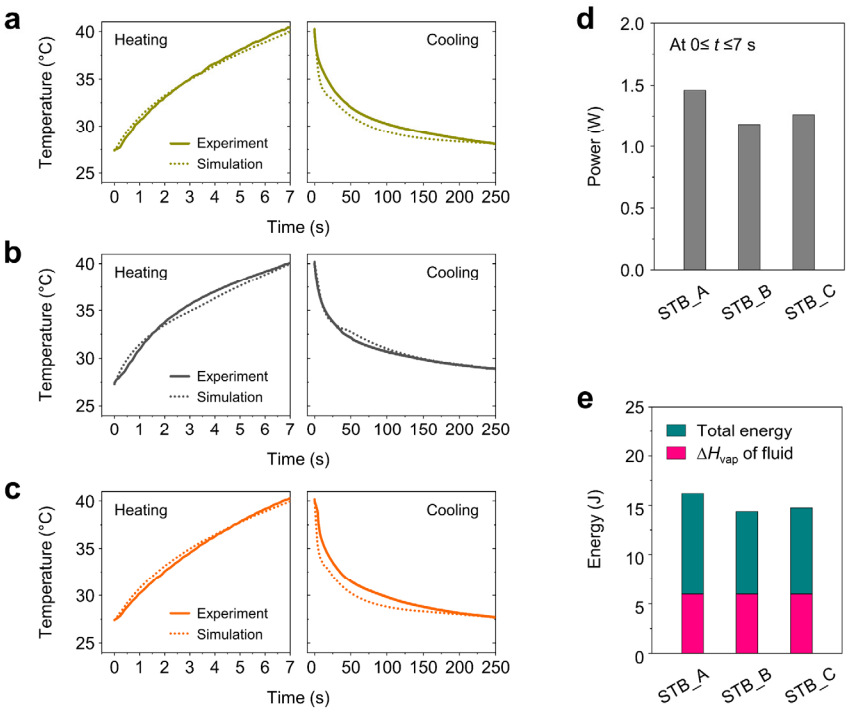

Fig. S24. (a–c) Temperature profile for heating (left panel) and cooling (right panel) for Case I using STB_A (a), STB_B (b), and STB_C (c). (d and e) Average power ($0 \leq t \leq 7$ s) needed to induce $\Delta T \approx 13$ °C (d), and total energy consumption ($0 \leq t \leq 7$ s) (e) for Case I using STB_A, STB_B, and STB_C, respectively. The applied voltage was 7.2, 5.0, and 6.8 V for STB_A, STB_B, and STB_C, respectively.

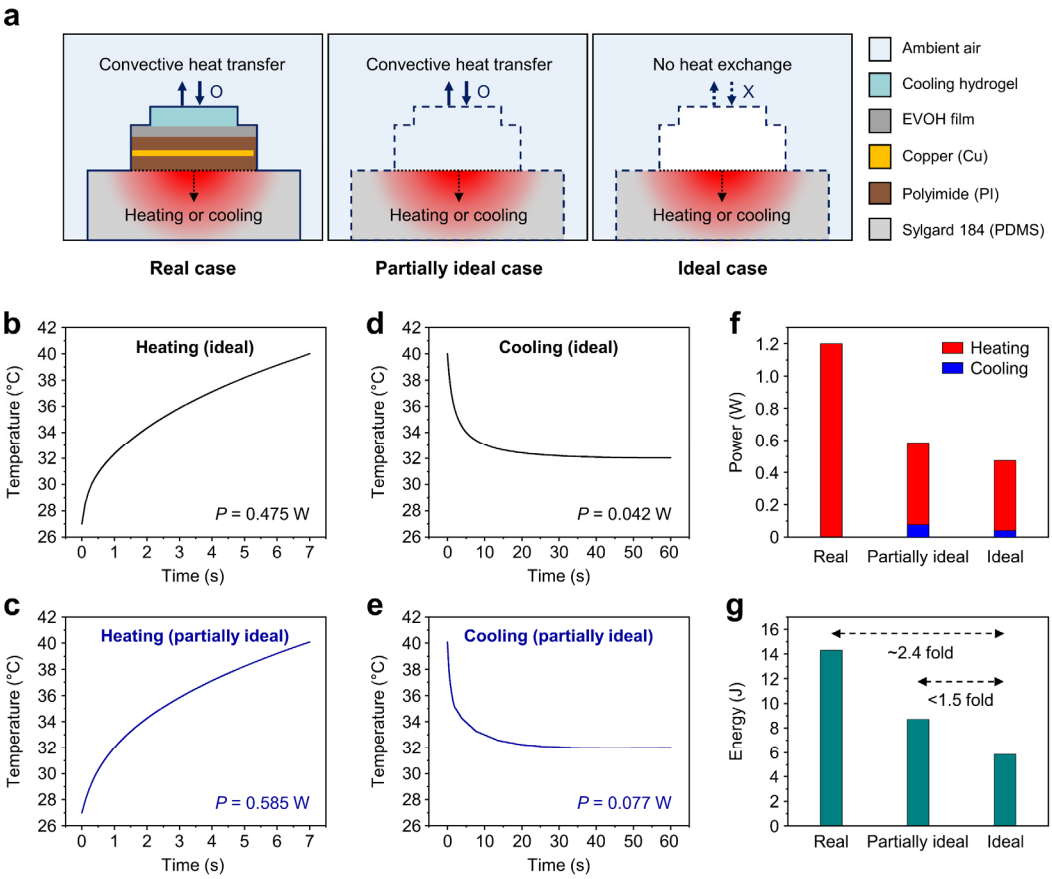

Fig. S25. (a) Side view model of a thermal module (Case I) for heating and cooling according to the real, partially ideal, and ideal cases in FEA simulations. The partially ideal case considers an ideal thermal module with negligible thickness and thermal mass and processes of parasitic heat loss such as cooling and radiation to ambient air (with a convective heat transfer coefficient, h = 10 W m^{-2} K^{-1}). The ideal case considers an ideal thermal module with negligible thickness and thermal mass and sets the boundary condition to an insulation with no heat exchange with ambient air, but only focuses on the boundary temperature at the skin phantom. (b and c) Temperature profile for heating (0≤ t ≤7 s) in ideal (b) and partially ideal case (c). (d and e) Temperature profile for cooling (0≤ t ≤60 s) in ideal (d) and partially ideal case (e). (f) The power required for heating the skin phantom from 27 °C to 40 °C (ΔT = 13 °C) within 7 s (red bar) and that for cooling the skin phantom from 40 °C to 32 °C (ΔT = –8 °C) within 60 s (blue bar) in ideal, partially ideal, and real case. (g) Total energy (power consumption) required to cycle the skin temperature from 27 °C to 40 °C by heating, and from 40 °C to 32 °C by cooling in ideal, partially ideal, and real case.

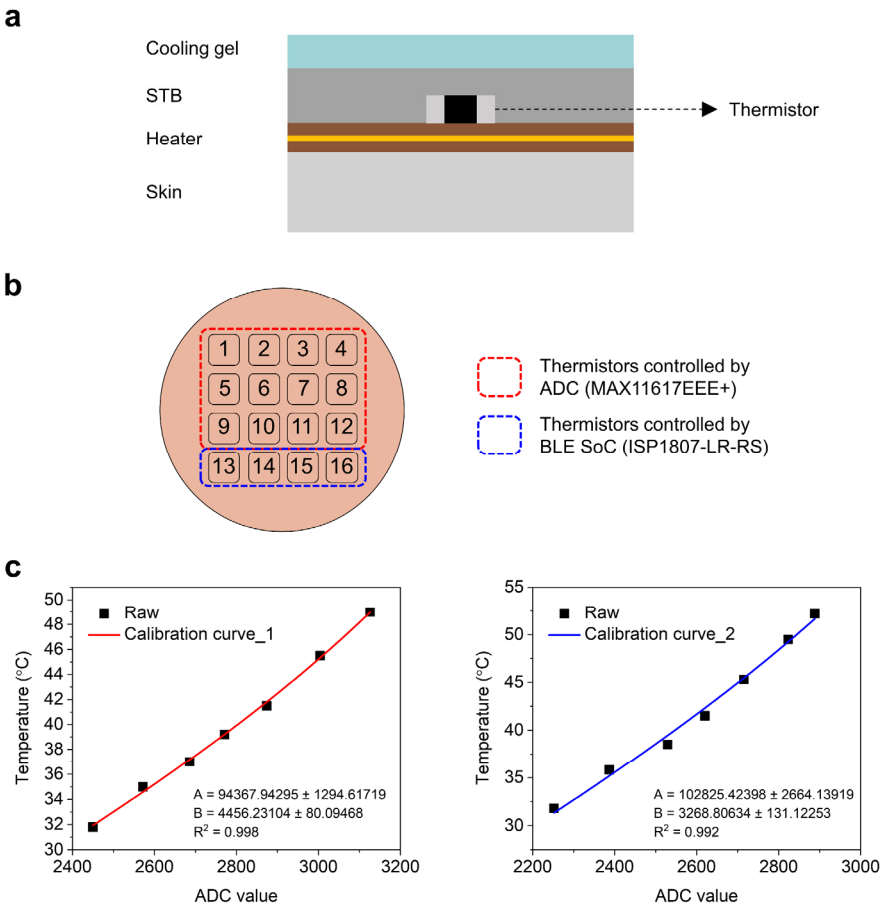

Fig. S26. (a) Side view schematic illustration for the calibration of the resistance of the thermistor. (b) Illustration of the device (4×4) where each number (1~16) represents the location of each thermal module. (c) Calibration curve for the thermistor controlled by ADC (red, calibration curve_1) and by BLE SoC (blue, calibration curve_2) using the following equation:

$$y = \frac{1}{\frac{1}{B} \times ln\left((4096 - x) \times \frac{100000}{A \times x}\right) + \frac{1}{25 + 273.15}} - 273.15 \qquad \text{Eq. S1}$$

where the *y* is temperature (°C), *x* is ADC value, and *A*, *B* are constants.

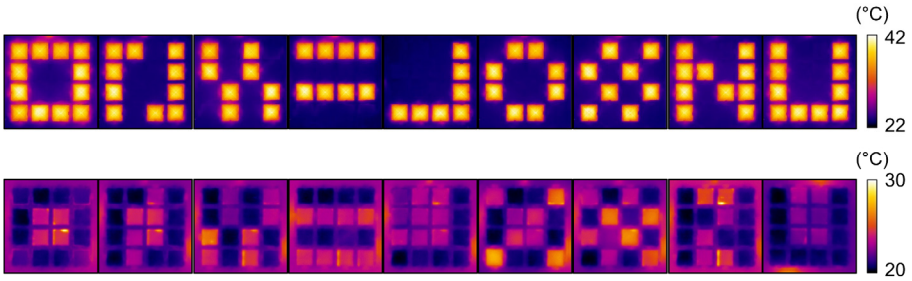

Fig. S27. Series of IR images of a device showing various thermal patterns initiated in heating (top panel) and cooling (bottom panel) modes.

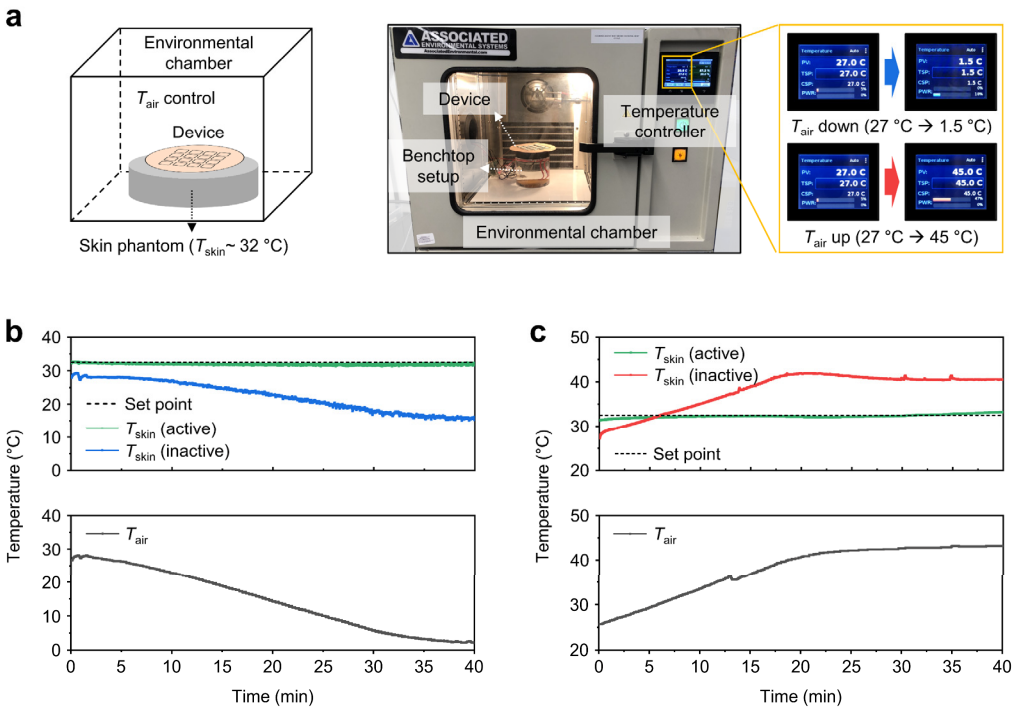

Fig. S28. (a) Schematic illustration and photograph of setups for testing thermoregulating performance of the t-eVR in an environmental chamber. The device is directly attached to a skin phantom at a temperature of 32 °C using the benchtop setup shown in Fig. S18 and S19. The temperature of the ambient air (T_{air}) in the chamber is controlled by a PID system. Two ambient conditions were examined: very low (T_{air}≈1.5 °C) or very high (T_{air}≈45 °C) temperatures. (b and c) Changes of skin (phantom) temperature (T_{skin}) in very cold air (T_{air}≈1.5 °C) (b), and very hot air (T_{air}≈45 °C) (c) with the system on/off on the skin phantom.

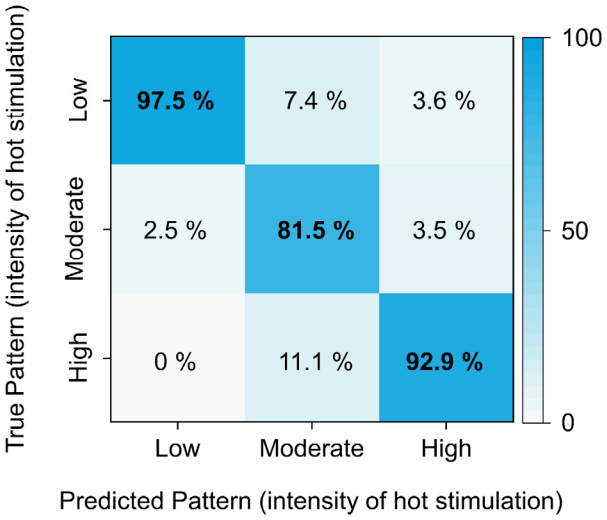

Fig. S29. Confusion matrix result for 150 blind tests for perception accuracy of different intensity of heating stimulation. Each level (low, moderate, and high) of stimulation was given by heating each participant's forearm to 30, 35, and 44 °C, respectively. The stimulation area was 8.33 cm^2 (4 heaters operated). Healthy adult volunteers (age 30–34 years; four male and one female healthy individuals) performed the test.

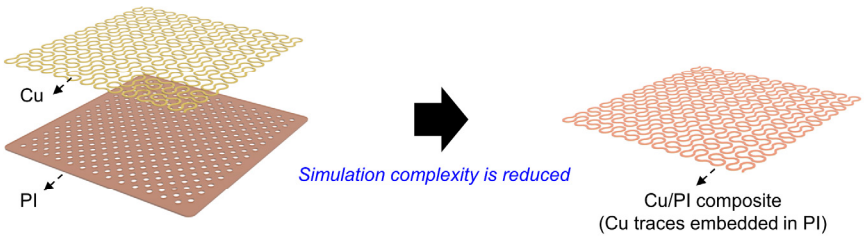

Fig. S30. Schematic illustration of the Peano fractal-shaped heater in real structure (separate Cu traces on a PI matrix) and effective structure (a Cu/PI composite). Simplifying the real structure into the effective structure reduces the complexity of the simulations.

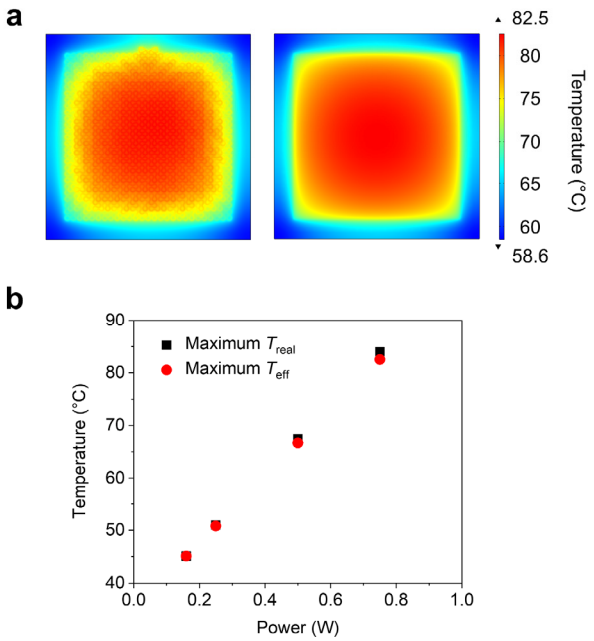

Fig. S31. (a) Finite element analysis (FEA) results for the Peano fractal-shaped heater (Cu/PI) that reveal its effective thermal properties. The results illustrate the real temperature distribution at the skin-interface (T_{real}, left), and the effective temperature distribution at the skin interface (T_{eff}, right). Effective properties for Cu/PI such as conductivity (k_{eff}), specific heat capacity ($C_{p,eff}$), and density (ρ_{eff}) were used in the simulation (k_{eff} = 10 W m^{-1} K^{-1}; $C_{p,eff}$ = 990 J kg^{-1} K^{-1}; and ρ_{eff} = 1496 kg m^{-3}). The applied power is 0.75 W. (b) Maximum temperature as a function of applied power.

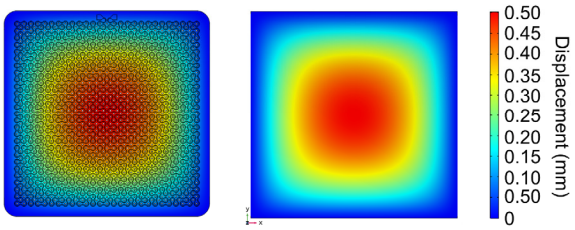

Fig. S32. Finite element analysis (FEA) result for the Peano fractal-shaped heater (Cu/PI) that shows the effective mechanical properties. The results illustrate the real displacement (d_{real}, left), and effective displacement (d_{eff}, right), respectively. With the use of effective elastic modulus (E_{eff}) of 2.1 GPa and Poisson's ratio (v) of 0.3, the maximum displacements for both d_{real} and d_{eff} are 0.5 mm at load of 40 kPa.

Table S1. Dimensions and thermal properties of materials (S8).

Parameters [unit]	Cooling gel	Alumized EVOH film	Polyimide (PI)	Heater (Cu/PI)	Sylgard 184 (PDMS)
Length [mm]	12.7	17.7	17.7	14.4	
Width [mm]	12.7	17.7	17.7	14.4	
Thermal conductivity [W m^{-1} K^{-1}]	0.59	0.36	0.12	10	0.2
Density [kg m^{-3}]	1000	1170	1420	1496	982
Specific heat capacity [J kg^{-1} K^{-1}]	4187	2400	1090	990	1615
Young's modulus [MPa]	0.1	1100	2500	2100	5.2
Poisson's ratio	0.4	0.3	0.34	0.3	0.4

Table S2. The effect of T_{skin} on $\dot{q}_{cooling}$ under free convection (v_{air} = 0 m s^{-1}). The dimensions of the cooling gel are the same for all conditions (length: 12.7×10^{-3} m, width: 12.7×10^{-3} m, and area: 0.161×10^{-3} m^2). Convective heat transfer coefficient of air was calculated in a condition that the T_{air} and relative humidity (RH) of the air distant from the cooling gel are 22 °C and 45 %, respectively.

h_{air} [W m^{-2} K^{-1}]	T_{skin} [°C]	$\dot{m}$ [g h^{-1}]	Q_{evap} [W]	$\|Q_{conv}\|$ [W]	T_{gel} [°C]	$\dot{q}_{cooling}$ [W m^{-2}]
14.8 ± 0.1	41.7 ± 0.4	~0.15	~0.10	~0.03	33.7 ± 0.2	450 ± 30
14.3 ± 0.1	38.8 ± 0.1	~0.13	~0.09	~0.02	32.2 ± 0.2	400 ± 10
13.3 ± 0.1	35.1 ± 0.2	~0.11	~0.08	~0.02	29.6 ± 0.3	370 ± 30
12.3 ± 0.1	32.0 ± 0.4	~0.09	~0.06	~0.01	27.6 ± 0.2	330 ± 10
10.8 ± 0.2	29.1 ± 0.2	~0.08	~0.06	< 0.01	25.4 ± 0.3	320 ± 20
7.5 ± 0.4	25.9 ± 0.1	~0.07	~0.05	< 0.01	22.8 ± 0.2	290 ± 30

Table S3. The effect of airflow velocity (v_{air}) on $\dot{q}_{cooling}$ under forced convection (v_{air} > 0 m s^{-1}). The dimensions of the cooling gel are the same for all conditions (length: 12.7×10^{-3} m, width: 12.7×10^{-3} m, and area: 0.161×10^{-3} m^2). The convective heat transfer coefficient of air was calculated in a condition that the T_{air} and relative humidity (RH) of the air distant from the cooling gel are 22 °C and 45 %, respectively.

v_{air} [m s^{-1}]	h_{air} [W m^{-2} K^{-1}]	T_{skin} [°C]	$\dot{m}$ [g h^{-1}]	Q_{evap} [W]	$\|Q_{conv}\|$ [W]	T_{gel} [°C]	$\dot{q}_{cooling}$ [W m^{-2}]
~1.3	32.8 ± 0.4	32.4 ± 0.2	~0.19	~0.13	< 0.01	23.7 ± 0.2	790 ± 60
~1.0	29.8 ± 0.2	32.3 ± 0.2	~0.18	~0.12	< 0.01	22.9 ± 0.5	750 ± 60
~0.6	22.4 ± 0.5	32.2 ± 0.1	~0.17	~0.11	< 0.01	22.8 ± 0.5	710 ± 30
~0.2	14.3 ± 0.6	32.4 ± 0.1	~0.15	~0.10	< 0.01	23.9 ± 0.7	620 ± 20
0.0	12.3 ± 0.1	32.0 ± 0.4	~0.09	~0.06	~0.01	27.6 ± 0.2	330 ± 10

Table S4. The effect of relative humidity (*RH*) on $\dot{q}_{cooling}$ under forced convection (v_{air}≈1.3 m s^{-1}). The dimensions of the cooling gel are the same for all conditions (length: 12.7×10^{-3} m, width: 12.7×10^{-3} m, and area: 0.161×10^{-3} m^2). The convective heat transfer coefficient of air was calculated in a condition that the T_{air} of the air distant from the cooling gel is 25 °C.

RH [%]	h_{air} [W m^{-2} K^{-1}]	T_{skin} [°C]	$\dot{m}$ [g h^{-1}]	Q_{evap} [W]	$\lvert Q_{conv} \rvert$ [W]	T_{gel} [°C]	$\dot{q}_{cooling}$ [W m^{-2}]
20	~33.4	28.4 ± 0.2	~0.23	~0.16	~0.02	21.2 ± 0.1	1100 ± 40
40	~33.4	27.7 ± 0.3	~0.18	~0.12	~0.02	21.5 ± 0.2	880 ± 40
60	~33.4	28.4 ± 0.3	~0.16	~0.11	< 0.01	24.1 ± 0.1	690 ± 20

Table S5. The effect of T_{air} on $\dot{q}_{cooling}$ under forced convection (v_{air}≈1.3 m s^{-1}). The dimensions of the cooling gel are the same for all conditions (length: 12.7×10^{-3} m, width: 12.7×10^{-3} m, and area: 0.161×10^{-3} m^2). The convective heat transfer coefficient of air was calculated in a condition that the *RH* of the air distant from the cooling gel is 40 %.

T_{air} [°C]	h_{air} [W m^{-2} K^{-1}]	T_{skin} [°C]	$\dot{m}$ [g h^{-1}]	Q_{evap} [W]	$\|Q_{conv}\|$ [W]	T_{gel} [°C]	$\dot{q}_{cooling}$ [W m^{-2}]
15	~33.5	20.4 ± 0.6	~0.16	~0.11	< 0.01	15.7 ± 0.4	660 ± 10
20	~33.5	25.4 ± 0.2	~0.17	~0.11	< 0.01	20.0 ± 0.1	720 ± 70
25	~33.4	27.7 ± 0.3	~0.18	~0.12	~0.02	21.5 ± 0.2	880 ± 40
30	~33.4	32.5 ± 0.3	~0.19	~0.13	~0.02	25.7 ± 0.1	940 ± 20
35	~33.3	35.9 ± 1.0	~0.20	~0.14	~0.03	28.6 ± 0.1	1100 ± 10

Movie S1 (separate file). Long-range delivery of spatiotemporal thermal pattern.

Movie S2 (separate file). Sensory expansion for thermal recognition of remote objects.

SI References

S1. R. Niiyama, D. Rus, S. Kim, “Pouch Motors: Printable/inflatable soft actuators for robotics” in *2014 IEEE International Conference on Robotics and Automation (ICRA)*, pp. 6332–6337.

S2. K. Narumi et al., Liquid Pouch Motors: Printable planar actuators driven by liquid-to-gas phase change for shape-changing interfaces, *IEEE Robotics and Automation Letters* **5**, 3915–3922 (2020).

S3. Technical Data Sheet for “3M™ Novec™ 7000 Engineered Fluid” available at https://multimedia.3m.com/mws/media/121372O/3m-novec-7000-engineered-fluid-tds.pdf.

S4. T. Bertrand, J. Peixinho, S. Mukhopadhyay, C. W. MacMinn, Dynamics of swelling and drying in a spherical gel, *Phys. Rev. Appl.* **6**, 064010 (2016).

S5. Data (heat of evaporation of water) available at https://www.engineeringtoolbox.com/water-properties-d_1573.html.

S6. M. Luo *et al.* High-density thermal sensitivity maps of the human body, *Build. Environ.* **167**, 106435 (2020).

S7. H. Hensel, “Cutaneous thermoreceptors” in *Handbook of Sensory Physiology, Volume 2: Somatosensory System*, A. Iggo, Eds. (Springer-Verlag, 1973), pp. 81.

S8. S. Pu *et al.*, Bioinspired sweating with temperature sensitive hydrogel to passively dissipate heat from high-end wearable electronics, *Energy Convers. Manag.* **180**, 747–756 (2019).